# Impact of interchannel misalignment on the performance of demosaicing algorithms dedicated to polarization images

Ronan Dumoulin[a], Pierre-Jean Lapray[a], Alban Foulonneau[a], and Laurent Bigué[a]

[a]Université de Haute-Alsace, IRIMAS UR 7499, Mulhouse, France

## ABSTRACT

Thanks to some technical progress in filter array technologies, capturing multimodal data of a scene, such as polarization and/or spectral information, in a single acquisition is possible. Nevertheless, a reconstruction procedure referred to as demosaicing is required to produce the various full definition images in each band. The computational imaging community often needs full-reference images to assess the performance of these reconstruction algorithms. Nevertheless, these multidimensional data are increasingly complex to capture, as the number of channels increases in the image. This often leads to misalignment among channels or noise introduced by imperfect optics. In this work, we propose a study on the use of these imperfect data in the context of demosaicing. The impact of misalignment is assessed on an existing Color Polarization Filter Array database, from which we demosaic the data using three types of demosaicing algorithms and use either pre-processed or raw dataset. We found that denoising and registration do not modify the hierarchy of best performing algorithms in case of sub-pixel shifts. We also show that visual artifacts, usually attributed to drawbacks of training-based demosaicing algorithms, may instead be due to the use of unregistered images during the training stage of the algorithms.

**Keywords:** Color and polarization imaging, demosaicing, registration

## 1. INTRODUCTION

Recent advances in imaging technologies allow capturing multimodal data, such as polarization or spectral images. Most commercial systems use a Polarization Filter Array (PFA) which produces single-band mosaiced images. In order to get the desired spectropolarimetric information, a reconstruction algorithm must be used. Proposing efficient reconstruction algorithms in the case where the information is rich (many polarization and/or spectral channels) is a very active research field. To evaluate the performance of these reconstruction algorithms, e.g. for image demosaicing or super-resolution, most existing works use genuine full-definition reference images for the definition of models by data, testing of algorithms or comparative analysis. These full-definition reference images shall not be produced using mosaiced sensors. But these data are increasingly complex to capture, as the number of channels increases. As an example, for spectropolarimetric data produced by CPFA (Color Polarization Filter Array) sensors, the images consist of 12 full-definition channels, where each channel captures an intensity relatively to a specific spectral band (red, green or blue) and a specific direction of polarization (typically $0°, 45°, 90°, 135°$). To capture the corresponding images at full definition, it is necessary to use complex but imperfect acquisition systems, such as a three-sensor camera coupled with additional optical elements, e.g. a rotating polarizer. As a result, full-definition images may contain spatially misaligned channels and/or noisy data. In this context, even a slight misregistration (less than 0.1 pixel)[1] can cause noticeable polarization artifacts.

Demosaicing algorithms dedicated to CPFA sensors often use inter-channel correlation for image reconstruction, which can be affected by poor alignment. However, as these databases are widely used in the context of computational imaging, it is natural to wonder whether these imperfect data are a bias in evaluating the performance of reconstruction algorithms such as demosaicing.

A recent review evaluates the pixel shift among several polarization images datasets[3] due to misalignment. It also investigates qualitatively the impact when visualizing the degree of linear polarization ($DoLP$) images

Further author information: (Send correspondence to Pierre-Jean Lapray)
Pierre-Jean Lapray: E-mail: pierre-jean.lapray@uha.fr, Telephone: +33 3 89 33 69 58

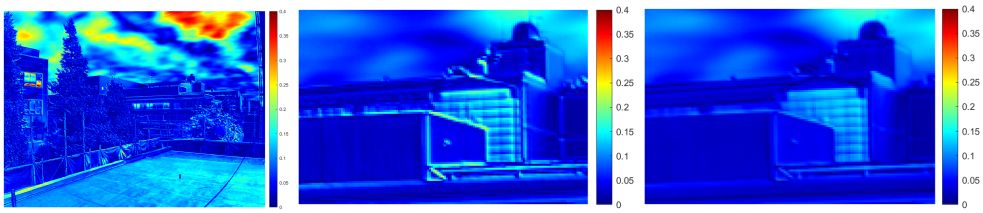

(a) *DoLP* (b) *DoLP* zoomed (c) *DoLP* after denoising and channel registration

Figure 1: Effect of the pre-processing applied to polarization images in this work. The degree of polarization (*DoLP*) images are computed from a set of four different intensity channels. A data preparation step is applied to compensate for possible alignment errors among channels and noise introduced by the measurement system. The image is from the dataset by Morimatsu *et al.*[2]

and the angle of polarization (*AoP*) images. In Figure 1, we can see that misalignment between polarization intensity images creates edge artifacts in the reconstructed *DoLP* image. Whereas some authors stress the point in registering the different bands,[4] these datasets are often considered as defect-free, and used as it is (without any pre-processing) for benchmarking algorithms or training machine learning algorithms. Up to our knowledge, no study has been done on the impact of using imperfect data for these operations.

In this paper, we investigate whether the use of unregistered data can lead to a potential misinterpretation of the performance of CPFA demosaicing algorithms.

In Section 2, we first recall the polarization basics. In Section 3, the experimental protocol used in this work is presented. In Section 4, we present and analyze the results quantitatively and qualitatively, before concluding in Section 5.

## 2. POLARIZATION BASICS

The Stokes vector is used to represent the state of polarization. In the case of linear polarization, it can be reduced to its first three components. The fourth component is used for circular polarization, which is not measured by current commercial CPFAs. Assuming that polarization images are commonly captured with a polarizer oriented at $\{0°, 45°, 90°, 135°\}$, the first three components of the Stokes vector $\boldsymbol{S}$ can be estimated from intensity images using the following equation:

$$S = \begin{bmatrix} S_0 \\ S_1 \\ S_2 \end{bmatrix} = \begin{bmatrix} (I_0 + I_{45} + I_{90} + I_{135})/2 \\ I_0 - I_{90} \\ I_{45} - I_{135} \end{bmatrix} \tag{1}$$

Degree of Linear Polarization (*DoLP*) and Angle of Polarization (*AoP*) can be computed using:

$$DoLP = \frac{\sqrt{S_1^2 + S_2^2}}{S_0} \qquad AoP = \frac{1}{2} arctan\left(\frac{S_2}{S_1}\right) \tag{2}$$

In case of color polarization imaging, the Stokes vectors, *DoLP* and *AoP* are computed for each spectral band.

## 3. EXPERIMENTAL PROTOCOL

Figure 2 shows an overview of the experimental protocol used in this work. The goal is to evaluate the impact of using either a raw database, or a database where the images have been pre-processed (denoising and channel registration), on the demosaicing algorithm ranking.

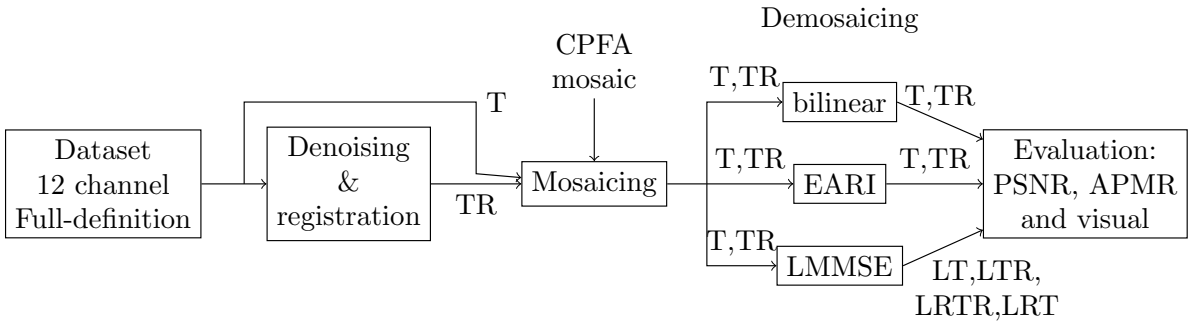


Figure 2: Overview of the experimental protocol used in this paper. T/TR correspond to images without/with denoising and registration. LT/LTR/LRTR/LRT correspond to the four scenarios of LMMSE presented in subsection 3.3.

### 3.1 Dataset

In this work, we use an image database from Morimatsu *et al.*[2] We chose this dataset because it is one of the existing datasets where full definition images are produced by sensors not using any micro-filters, i.e. non interpolated ground-truth data. It is composed of 40 spectropolarimetric images, with a pixel depth of 10-bit and a definition of $1024 \times 768$ pixels. The images are composed by 12 full-definition channels, and the channels are a combination of three color channels ($c \in \{R, G, B\}$) and four polarization angles of analysis, equally distributed between 0° and 180° ($p \in \{0°, 45°, 90°, 135°\}$). Channels are referred to as $I_{p,c}$. Scenes from this database have been captured with a three-CCD RGB camera equipped with a rotating polarizer used in four orientations. As mentioned in Bigué *et al.*,[3] images exhibit spatial shifts between channels of the order of 0.2 pixels on average. Some edge artifacts may appear and are caused by these spatial shifts. The artifacts are particularly visible in $DoLP$ or $AoP$ images, as can be seen in Fig. 3.

### 3.2 Method for denoising and channel registration

Here, we prepare the images of the database, by following the procedure used by Li *et al.*[5] The only difference with this work is that we apply pre-processing on images with 12 channels (i.e. we have color polarization images) instead of 4 channels (polarization images). These steps are intended to improve the quality of spectropolarimetric images.

The first step applies a denoising procedure to the channels by using Block-Matching and 3-D filtering (BM3D[6]). Each channel is denoised independently. The second step estimates and corrects the spatial shifts between the 12 channels by using a subpixel image registration algorithm presented by Guizar-Sicairos *et al.*[7] This is a frequency domain algorithm which estimates the linear phase difference between the Fourier transforms of the images. The shift is restricted to a uniform rigid translation. The channel $I_{0,R}$ is arbitrarily chosen as a fixed reference, and all other channels are aligned with respect to it.

### 3.3 Method for benchmarking

To study the impact of data preparation on the evaluation of demosaicing algorithm, we use two experiments with two different goals. The aim of the first experiment is to see the effect of the data preparation on the ranking performance of three algorithms. The second protocol tests different scenarios for a machine learning demosaicing algorithm, i.e. the model selection is done using either processed or unprocessed data.

The two datasets (raw and pre-processed) are mosaiced to simulate CPFA images. The mosaic used for mosaicing corresponds to the mosaic of Sony's sensors.[8] It is a 12-channel sensor, which combines three color filters arranged in a Quad Bayer spatial arrangement,[9] and four polarization angles of analysis equally distributed between 0° and 180° ($\theta = 0°, 45°, 90°, 135°$).[10] For each pixel position, only one intensity measurement out of the twelve channels is made, therefore the other eleven channel values are missing.

For the first experiment, we selected three interpolation algorithms to interpolate spatially the spectropolarimetric data: bilinear interpolation, Edge-Aware Residual Interpolation[2] (EARI), and Linear Minimum Mean

Square Error (LMMSE) algorithm.[11,12] LMMSE is a machine learning algorithm, which means that it requires a training stage before demosaicing. As shown in a previous work,[11] 12 images are enough for the learning procedure of the algorithm. For a fair comparison with other algorithms, we decided to split the dataset into two parts, a set of 12 images for training and the remaining 28 images for testing algorithms. To summarize, the same 28 images of both initial dataset and processed dataset are demosaiced by bilinear, EARI and LMMSE algorithms.

The second experiment focusses only on the performance of the machine learning algorithm (LMMSE). We define four scenarios for training and testing the LMMSE algorithm:

- $(L, T)$: learning and test with initial dataset
- $(L_R, T_R)$: learning and test with denoised and registered dataset
- $(L, T_R)$: learning with initial dataset and test with denoised and registered dataset
- $(L_R, T)$: learning with denoised and registered dataset and test with initial dataset

In the case of the first experiment, the only two scenarios which are compared with the other algorithms are $(L, T)$ and $(L_R, T_R)$.

### 3.4 Metrics

To quantify the results obtained for the two experiments described above, we use two objective metrics. The first is the PSNR (Peak Signal-to-Noise Ratio), which is a reference-based metric. We use the 2 databases for the computation of the PSNR, the one without pre-processing and the other one with pre-processing. The reference used in PSNR is selected depending on the origin of the image to be demosaiced.

The second metric is the Accuracy of Polarization Measurement Redundancy[5] (APMR). APMR is a no-reference quality metric dedicated to polarimetric images. This metric is based on the polarization information redundancy when we have four polarization intensity measurements ($0°, 45°, 90°$, and $135°$). Thanks to this redundancy, we can estimate the $S_0$ component of the Stokes vector in two ways:

$$\begin{cases} S_0 = I_0 + I_{90} & (3) \\ S_0 = I_{45} + I_{135} & (4) \end{cases}$$

These ways of computing $S_0$ should lead to the same value in case of perfect data, i.e. channels being free of noise and aligned. To evaluate the quality of polarimetric data, the metric computes the relative error $R$ between $S_0$ given by the Eq.(3) and Eq.(4). Then, this error is normalized to compute the Mean Absolute energy of R (MAR):

$$MAR = \frac{\sum_{i=1}^{h} \sum_{j=1}^{w} R_{i,j}^2}{h \times w} \ , \tag{5}$$

where $h$ and $w$ are the image dimensions, and $R_{i,j} = I_{0,i,j} + I_{90,i,j} - I_{45,i,j} - I_{135,i,j}$.

Finally, $APMR$ is obtained using the following equation:

$$APMR = 10 \log_{10} \left( \frac{(2^k - 1)^2}{MAR} \right) \ , \tag{6}$$

with $k$ the bit depth of the image. Authors showed that APMR is correlated with other reference metrics,[5] such as Peak Signal to Noise Ratio (PSNR) or Structural Similarity Index Measure (SSIM). We use this metric to quantify the quality improvement obtained by the data preparation done in Section 3.2. As APMR is developed for monochrome polarimetric images, we compute the APMR for the three spectral bands (red, green and blue) independently.

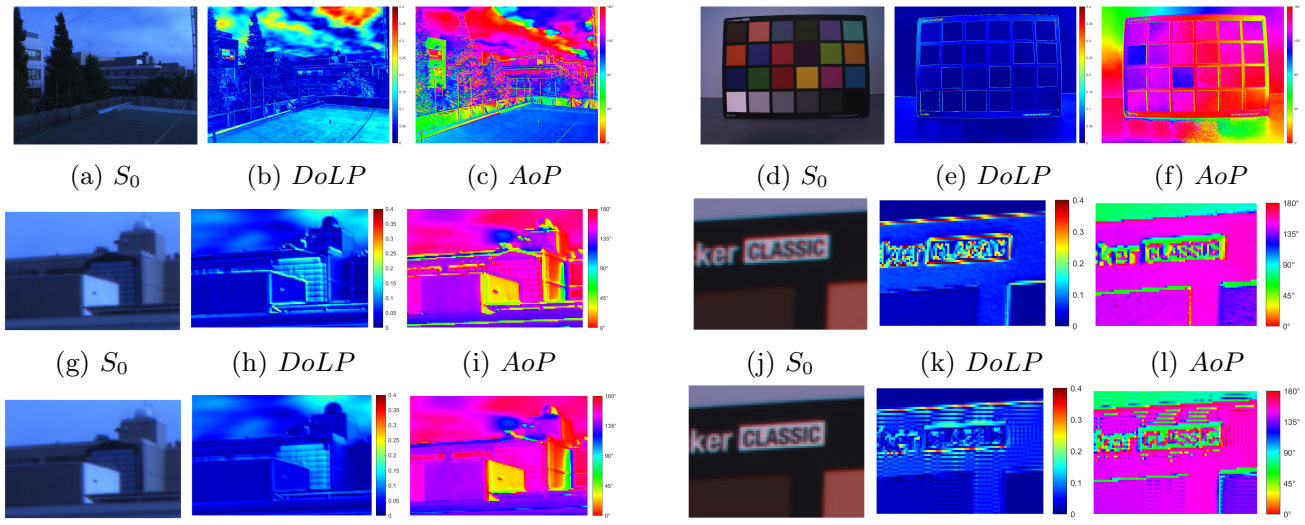

(a) $S_0$ (b) $DoLP$ (c) $AoP$ (d) $S_0$ (e) $DoLP$ (f) $AoP$

(g) $S_0$ (h) $DoLP$ (i) $AoP$ (j) $S_0$ (k) $DoLP$ (l) $AoP$

(m) $S_0$ (n) $DoLP$ (o) $AoP$ (p) $S_0$ (q) $DoLP$ (r) $AoP$

Figure 3: Image 'outside' on left and 'chart' on right. $DoLP$ and $AoP$ images are shown for the green band. First row shows the images without applying the denoising and channel registration operations. Second row are the zoomed versions. Third row are the zoomed version of images after applying the denoising and channel registration algorithms.

## 4. RESULTS AND ANALYSIS

### 4.1 Effect of denoising and channel registration

Table 1: Average $\mu$ and standard deviation $\sigma$ of APMR for complete dataset without and with denoising and registration. Best mean values by spectral channel are highlighted in bold fonts. APMR is computed on the image without the borders (border size of 4 pixels).

| | **Without denoising and registration** | | **With denoising and registration** | |
|---|---|---|---|---|
| | $\mu$ | $\sigma$ | $\mu$ | $\sigma$ |
| $I_R$ | 43.19 | 6.64 | **43.66** | 6.12 |
| $I_G$ | 44.42 | 7.15 | **44.71** | 6.61 |
| $I_B$ | 43.96 | 6.82 | **44.32** | 6.47 |

Table 1 shows the mean of APMR for the 40 images of the Morimatsu dataset before and after denoising and registration. The improvement of APMR shows that the quality of the 40 images is slightly improved.

Figure 3 shows a zoom on the scenes called 'outside' and 'chart'. Zoom of $S_0$ are visually very similar. When zooming, $DoLP$ and $AoP$ exhibit some artifacts due to misalignment. This has been largely reduced by applying the channel registration step. Nevertheless, when zooming in the 'chart' image, we can see that the registration algorithm applied to intensity images creates some artifacts on $DoLP$ and $AoP$ images: a small ripple effect in intensity is amplified in the computation of $DoLP$ and $AoP$.

### 4.2 Ranking of demosaicing algorithms

Table 2 shows the average PSNR and standard deviations for the 28 demosaiced images. First, we can see a clear hierarchy among demosaicing algorithms, which is the same whether the data are denoised and registered or not. Bilinear interpolation is the less performing solution, EARI algorithm performs significantly better and finally LMMSE performs best. Applying denoising and registration provides significant improvement (for EARI $+1.23dB$ and $+1.09dB$ for LMMSE), except for bilinear interpolation ($+0.42dB$), which is not that surprising since bilinear interpolation processes the various channels separately. On the opposite, EARI and LMMSE simultaneously deal with several channels, supposed to be aligned, and then these techniques are more efficient

Table 2: Average $\mu$ and standard deviation $\sigma$ of PSNR for bilinear, EARI and LMMSE algorithms without and with denoising and registration. Best mean values by channel are highlighted in bold fonts. PSNR is computed on the image without the borders (border size of 4 pixels).

| | **bilinear** | | | | **EARI** | | | | **LMMSE** | | | |
|---|---|---|---|---|---|---|---|---|---|---|---|---|
| | **w/o denoising & registration** | | **with denoising & registration** | | **w/o denoising & registration** | | **with denoising & registration** | | $(L,T)$ | | $(L_R,T_R)$ | |
| | $\mu$ | $\sigma$ | $\mu$ | $\sigma$ | $\mu$ | $\sigma$ | $\mu$ | $\sigma$ | $\mu$ | $\sigma$ | $\mu$ | $\sigma$ |
| $I_{0,R}$ | 35.36 | 4.45 | 35.74 | 4.67 | 38.15 | 4.48 | 39.27 | 5.03 | 39.65 | 3.85 | **40.52** | 4.19 |
| $I_{0,G}$ | 38.11 | 4.38 | 38.58 | 4.40 | 43.58 | 4.53 | 45.02 | 4.84 | 44.47 | 4.19 | **46.12** | 4.41 |
| $I_{0,B}$ | 36.10 | 4.88 | 36.47 | 4.97 | 40.99 | 5.14 | 41.96 | 5.38 | 41.26 | 4.77 | **41.68** | 4.64 |
| $I_{45,R}$ | 35.04 | 4.43 | 35.45 | 4.61 | 37.64 | 4.55 | 38.84 | 5.01 | 39.33 | 3.82 | **40.12** | 3.96 |
| $I_{45,G}$ | 37.66 | 4.35 | 38.16 | 4.44 | 42.49 | 4.64 | 44.23 | 5.03 | 43.72 | 4.45 | **45.47** | 4.39 |
| $I_{45,B}$ | 35.71 | 4.92 | 36.09 | 5.07 | 40.29 | 5.28 | 41.29 | 5.40 | 40.55 | 4.77 | **41.07** | 4.72 |
| $I_{90,R}$ | 35.47 | 4.42 | 35.85 | 4.60 | 38.23 | 4.48 | 39.36 | 5.00 | 39.84 | 3.91 | **40.69** | 4.30 |
| $I_{90,G}$ | 38.20 | 4.43 | 38.67 | 4.50 | 43.80 | 4.63 | 45.16 | 4.98 | 44.75 | 4.27 | **46.40** | 4.54 |
| $I_{90,B}$ | 36.10 | 4.92 | 36.48 | 5.03 | 41.11 | 5.27 | 41.95 | 5.34 | 41.16 | 4.60 | **41.88** | 4.79 |
| $I_{135,R}$ | 35.10 | 4.48 | 35.49 | 4.67 | 37.68 | 4.49 | 38.84 | 5.05 | 39.03 | 3.89 | **40.09** | 4.25 |
| $I_{135,G}$ | 37.71 | 4.41 | 38.18 | 4.45 | 42.42 | 4.70 | 44.14 | 5.02 | 43.17 | 4.41 | **45.13** | 4.64 |
| $I_{135,B}$ | 35.75 | 4.89 | 36.13 | 4.96 | 40.32 | 5.42 | 41.40 | 5.50 | 40.42 | 4.79 | **41.18** | 4.80 |
| $I_{tot}$ | 36.36 | 4.44 | 36.78 | 4.54 | 40.56 | 4.66 | 41.79 | 4.97 | 41.44 | 4.22 | **42.53** | 4.40 |
| $S_0$ | 37.32 | 4.35 | 37.40 | 4.345 | 41.38 | 4.57 | 42.09 | 4.97 | 42.34 | 4.31 | **42.84** | 4.60 |
| $S_1$ | 43.34 | 4.37 | 43.91 | 4.44 | 47.21 | 4.61 | 48.56 | 4.88 | 48.73 | 3.84 | **49.98** | 3.76 |
| $S_2$ | 41.75 | 4.69 | 43.34 | 4.45 | 44.97 | 4.90 | 47.56 | 4.91 | 45.70 | 4.18 | **49.05** | 3.82 |

Table 3: Average $\mu$ and standard deviation $\sigma$ of APMR for full definition reference and images demosaiced with bilinear interpolation or EARI algorithm without and with denoising and registration. APMR is computed on the image without 4-pixels thick borders.

| | **reference** | | | | **bilinear** | | | | **EARI** | | | |
|---|---|---|---|---|---|---|---|---|---|---|---|---|
| | **w/o denoising & registration** | | **with denoising & registration** | | **w/o denoising & registration** | | **with denoising & registration** | | **w/o denoising & registration** | | **with denoising & registration** | |
| | $\mu$ | $\sigma$ | $\mu$ | $\sigma$ | $\mu$ | $\sigma$ | $\mu$ | $\sigma$ | $\mu$ | $\sigma$ | $\mu$ | $\sigma$ |
| $I_R$ | 44.28 | 6.61 | 44.43 | 6.21 | 38.79 | 4.86 | 41.39 | 5.51 | 38.28 | 4.71 | 40.72 | 5.29 |
| $I_G$ | 45.61 | 7.20 | 45.48 | 6.79 | 35.77 | 4.99 | 37.03 | 5.18 | 39.40 | 5.42 | 41.66 | 5.75 |
| $I_B$ | 45.10 | 6.58 | 44.93 | 6.38 | 39.66 | 5.38 | 41.98 | 5.70 | 39.54 | 5.03 | 41.87 | 5.42 |

if the data are indeed correctly aligned. The improvement can be as high as $1.5dB$ on intensity images and then propagates to Stokes components.

Table 3 shows the APMR results for the 28 demosaiced images and corresponding reference images, demosaiced by bilinear and EARI algorithms, without and with denoising and registration. The results for LMMSE algorithm are shown in Table 4. At first, we can note that for reference images, APMR does not increase significantly when denoising and registration are applied. For demosaiced images, denoising and registration provides a significantly higher APMR. Whereas PSNR showed the superiority of EARI over bilinear interpolation, it is not so clear regarding APMR. In our specific case, it is to note that we do not see the correlation between APMR and PSNR demonstrated by the authors of the metric. On the example of Fig. 4, on $DoLP$ subimages, it appears clearly that demosaicing with EARI provides better results than demosaicing with bilinear interpolation. Anyway, demosaicing using LMMSE provides superior performance over all other algorithms, indicated by PSNR, APMR and as can be verified in Fig. 4. The visual result is rather close to the original full-definition reference image.

Fig. 4 shows the reference image named 'cup2' and its demosaiced version by bilinear, EARI and LMMSE algorithms. First, we can see the changes between $DoLP$ and $AoP$ without and with denoising and registration. The $DoLP$ of some edges appear lower after denoising and registration. After denoising and alignment, the $AoP$ image of the bird becomes smoother, some edges disappear, and it seems that we get less variety of polarization

angles. The behavior of bilinear and EARI remains the same. For scenario $(L, T)$ and $(L_R, T_R)$ of LMMSE we can see that zipping artifacts appear lower (on the bird's wing for example).

To summarize, for the proposed experiment, we can see that the fact of denoising and registering images does not change the hierarchy of the best performing demosaicing algorithms. And we can notice that the correlation between PSNR and APMR is not total for the ranking of demosaicing algorithms. Visually, we can see that for LMMSE algorithm, the learning can reduce zipping artifacts.

### 4.3 Impact on learning

Table 4: Average $\mu$ and standard deviation $\sigma$ of APMR for LMMSE algorithms without and with denoising and registration. $(L/L_R)$ indicate learning images without/with denoising and registration, $(T/T_R)$ indicate test images without/with denoising and registration. APMR is computed on the image without 4-pixels thick borders.

| | **LMMSE** | | | | | | | |
|---|---|---|---|---|---|---|---|---|
| | $(L, T)$ | | $(L_R, T)$ | | $(L_R, T_R)$ | | $(L, T_R)$ | |
| | $\mu$ | $\sigma$ | $\mu$ | $\sigma$ | $\mu$ | $\sigma$ | $\mu$ | $\sigma$ |
| $I_R$ | 45.47 | 5.51 | 44.79 | 5.56 | 46.31 | 5.97 | 46.49 | 5.77 |
| $I_G$ | 46.03 | 5.57 | 45.68 | 5.69 | 47.00 | 5.99 | 46.92 | 5.79 |
| $I_B$ | 44.79 | 4.72 | 44.50 | 5.02 | 45.87 | 5.16 | 45.51 | 4.79 |

Table 5: Average $\mu$ and standard deviation $\sigma$ of PSNR for LMMSE algorithms. $(L/L_R)$ indicate learning images without/with denoising and registration, $(T/T_R)$ indicate test images without/with denoising and registration. PSNR is computed on the image without 4-pixels thick borders.

| | $\boldsymbol{I}_{tot}$ | | $\boldsymbol{S}_0$ | | $\boldsymbol{S}_1$ | | $\boldsymbol{S}_2$ | |
|---|---|---|---|---|---|---|---|---|
| | $\mu$ | $\sigma$ | $\mu$ | $\sigma$ | $\mu$ | $\sigma$ | $\mu$ | $\sigma$ |
| **LMMSE** $(L_R, T_R)$ | 42.53 | 4.40 | 42.84 | 4.60 | 49.98 | 3.76 | 49.05 | 3.82 |
| **LMMSE** $(L, T_R)$ | 41.88 | 4.36 | 42.44 | 4.57 | 49.63 | 3.68 | 46.91 | 3.81 |
| **LMMSE** $(L, T)$ | 41.44 | 4.22 | 42.34 | 4.31 | 48.73 | 3.84 | 45.70 | 4.18 |
| **LMMSE** $(L_R, T)$ | 40.99 | 4.22 | 41.89 | 4.27 | 48.44 | 3.92 | 45.22 | 4.29 |

Table 5 shows the average PSNR and standard deviations for the 28 images by LMMSE for the four scenarios. We can see that the two best results are for the scenarios $(L_R, T_R)$ and $(L, T_R)$. It can be explained by the fact that denoised and registered images have better spatial correlation (due to denoising) and better inter-channels correlation (due to registration). As the LMMSE assumes that there is strong correlation in the images, the scores of PSNRs are better. The scenario $(L_R, T_R)$ is better because during the learning, these higher correlations are taken into account. The worst scenario is $(L_R, T)$ because during the training, the correlations which are learned are higher than the correlations in the demosaiced images. In our case, we can see that LMMSE is relatively robust to the use of raw data for learning in terms of PSNR.

Table 4 shows the average APMR and standard deviations for the 28 images by LMMSE for the four scenarios. For the bands green and blue, we have the same ranking for the four scenarios as with PSNR. For the red band, the only difference is that the scenario $(L, T_R)$ is better than the scenario $(L_R, T_R)$.

On the Figure 4, we can see the $DoLP$ and $AoP$ of the four scenarios of LMMSE demosaicing. If we compare the scenarios, we can see that $DoLP$ and $AoP$ are smoother when the learning uses denoised and registered images. The learning with not denoised and registered images adds more zipping artifacts on demosaiced image.

To summarize, we can see, in terms of PSNR and APMR, that LMMSE is relatively robust to the use of non pre-processed images for training. Nevertheless, visually, we can notice that learning with pre-processed images gives smoother results, which seems physically more coherent in relation to the scene. Learning with non pre-processed images can give good results in terms of PSNR and APMR, but can produce visual artifacts.

(a) $S_0$ ref. (b) $DoLP$ ref. (c) $AoP$ ref.

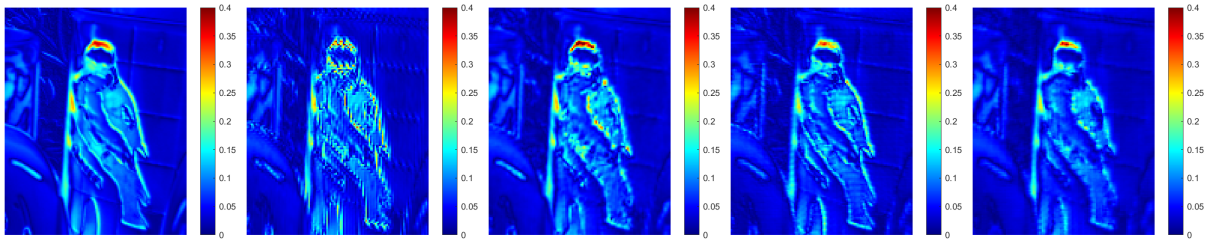

(d) ref., unreg. (e) bilinear, unreg. (f) EARI, unreg. (g) LMMSE $(L,T)$ (h) LMMSE $(L_R,T)$

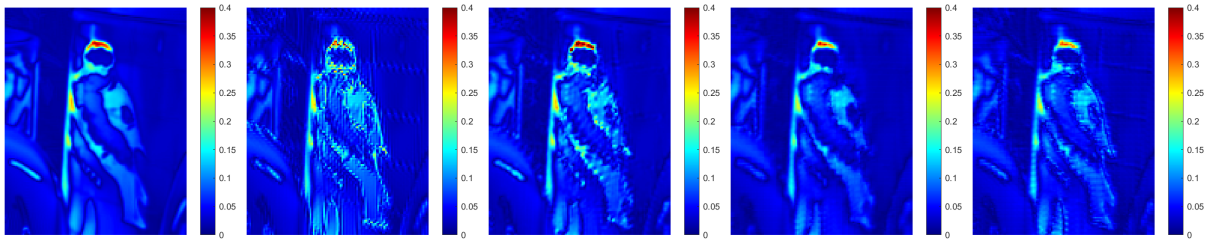

(i) ref., reg. (j) bilinear, reg. (k) EARI, reg. (l) LMMSE $(L_R,T_R)$ (m) LMMSE $(L,T_R)$

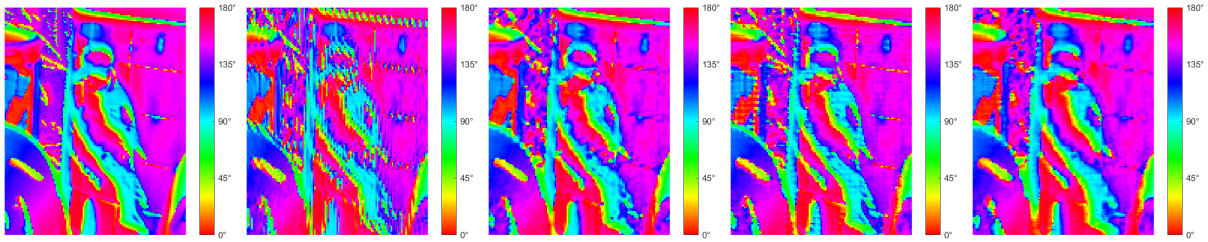

(n) ref., unreg. (o) bilinear, unreg. (p) EARI, unreg. (q) LMMSE $(L,T)$ (r) LMMSE $(L_R,T)$

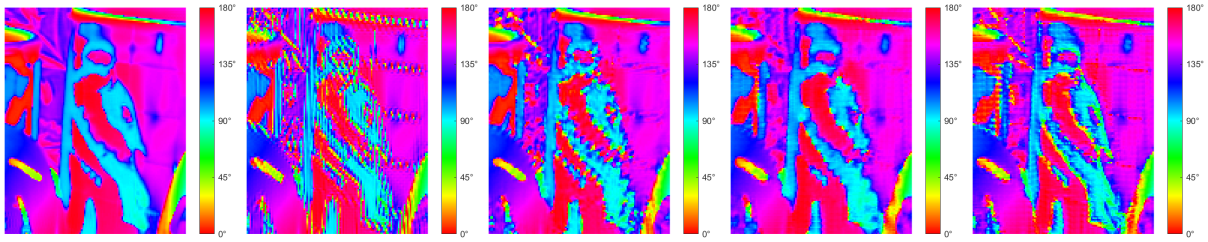

(s) ref., reg. (t) bilinear, reg. (u) EARI, reg. (v) LMMSE $(L_R,T_R)$ (w) LMMSE $(L,T_R)$

Figure 4: Image 'cup2', where $S_0$, $DoLP$ and $AoP$ are shows for the green band. (a/b/c) are the reference ($S_0/DoLP/AoP$) raw image. (d-h/n-r) correspond to images of ($DoLP/AoP$) without pre-processing, (i-m/s-w) correspond to images of ($DoLP/AoP$) with pre-processing. (d,i,n,s) are the reference, (e,j,o,t/f,k,p,u) are the demosaiced images by (bilinear/EARI). (g,q/l,v/h,r/m,w) are demosaiced images by LMMSE (learning and test on no pre-processing images/learning and test on pre-processing images/learning on pre-processing images and test on no pre-processing image/learning on no pre-processing images and test on pre-processing image).

## 5. CONCLUSION

We studied the impact of denoising and registration on the performance of three types of demosaicing algorithms in the field of spectropolarimetric imaging. As far as PSNR is concerned, denoising and registering images prior to demosaicing does not modify the hierarchy of best performing algorithms, with learning based LMMSE algorithm ranking at top. For EARI and LMMSE, prior denoising and registration increases PSNR of intensity images about $1dB$, which is interesting since this increase is still noticeable in the polarimetric metrics estimated from intensities. We also studied the impact of denoising and registration on the learning set of LMMSE algorithm. Performing denoising and registration on learning set is only worth if test images are also denoised and registered. It provides an average $1dB$ increase on intensity demosaiced images and final $DoLP$ images are visually very similar to reference images, almost free of visual artifacts.

## REFERENCES


[1] Smith, M., Woodruff, J., and Howe, J., "Beam wander considerations in imaging polarimetry," in [*SPIE's International Symposium on Optical Science, Engineering, and Instrumentation*], *Proc. SPIE* **3754** (1999).

[2] Morimatsu, M., Monno, Y., Tanaka, M., and Okutomi, M., "Monochrome and color polarization demosaicking using edge-aware residual interpolation," *2020 IEEE International Conference on Image Processing (ICIP)* , 2571–2575, IEEE, Abu Dhabi, United Arab Emirates (2020).

[3] Bigué, L., Foulonneau, A., and Lapray, P.-J., "Production of high-resolution reference polarization images from real world scenes," in [*Polarization Science and Remote Sensing XI*], Kupinski, M. K., Shaw, J. A., and Snik, F., eds., **12690**, 126900B, International Society for Optics and Photonics, SPIE (2023).

[4] Zeng, X., Luo, Y., Zhao, X., and Ye, W., "An end-to-end fully-convolutional neural network for division of focal plane sensors to reconstruct $S_0$, $DoLP$, and $AoP$," *Opt. Express* **27**, 8566–8577 (2019).

[5] Li, N., Teurnier, B. L., Boffety, M., Goudail, F., Zhao, Y., and Pan, Q., "No-reference physics-based quality assessment of polarization images and its application to demosaicking," *IEEE Transactions on Image Processing* **30**, 8983–8998 (2021).

[6] Dabov, K., Foi, A., Katkovnik, V., and Egiazarian, K., "Image denoising by sparse 3-d transform-domain collaborative filtering," *IEEE Transactions on Image Processing* **16**, 2080–2095 (Aug. 2007).

[7] Guizar-Sicairos, M., Thurman, S. T., and Fienup, J. R., "Efficient subpixel image registration algorithms," *Optics Letters* **33**, 156 (Jan. 2008).

[8] Sony, "Polarization image sensor," tech. rep., Polarsens (2018).

[9] Okawa, T., Ooki, S., Yamajo, H., et al., "A 1/2inch 48m all pdaf cmos image sensor using 0.8 $\mu$m quad bayer coding 2× 2ocl with 1.0 lux minimum af illuminance level," in [*International Electron Devices Meeting*], 16–3, IEEE (2019).

[10] Chun, C. S., Fleming, D. L., and Torok, E., "Polarization-sensitive thermal imaging," in [*Automatic Object Recognition IV*], **2234**, 275–286, International Society for Optics and Photonics (1994).

[11] Dumoulin, R., Lapray, P.-J., Thomas, J.-B., and Farup, I., "Impact of training data on lmmse demosaicing for colour-polarization filter array," in [*2022 16th International Conference on Signal-Image Technology & Internet-Based Systems (SITIS)*], IEEE (Oct. 2022).

[12] Spote, A., Lapray, P.-J., Thomas, J.-B., and Farup, I., "Joint demosaicing of colour and polarisation from filter arrays," in [*Color Imaging and Conference*], **29**(1), 288–293 (2021).